PROCEEDINGS A

royalsocietypublishing.org/journal/rspa

Research

Cite this article: Yadav S, Sagapuram D. 2020 Nucleation properties of isolated shear bands. *Proc. R. Soc. A* **476**: 20200529.
http://dx.doi.org/10.1098/rspa.2020.0529

Received: 7 July 2020
Accepted: 4 August 2020

Subject Areas:
materials science, mechanical engineering

Keywords:
shear bands, instability, nucleation, dislocations, metals

Author for correspondence:
Dinakar Sagapuram
e-mail: dinakar@tamu.edu

Nucleation properties of isolated shear bands

Shwetabh Yadav and Dinakar Sagapuram

Department of Industrial and Systems Engineering, Texas A&M University, College Station, TX 77843, USA

DS, 0000-0001-9248-5380

Shear banding, or localization of intense strains along narrow bands, is a plastic instability in solids with important implications for material failure in a wide range of materials and across length scales. In this article, we report on a series of experiments on the nucleation of single isolated shear bands in three model alloys. Nucleation kinetics of isolated bands and characteristic stresses are studied using high-speed *in situ* imaging and parallel force measurements. The results demonstrate the existence of a critical shear stress required for band nucleation. The nucleation stress bears little dependence on the normal stress and is proportional to the shear modulus. These properties are quite akin to those governing the onset of dislocation slip in crystalline solids. A change in the flow mode from shear banding to homogeneous plastic flow occurs at stress levels below the nucleation stress. Phase diagrams delineating the strain, strain rate and temperature domains where these two contrasting flow modes occur are presented. Our work enables interpretation of shear band nucleation as a crystal lattice instability due to (stress-assisted) breakdown of dislocation barriers, with quantitative experimental support in terms of stresses and the activation energy.

1. Introduction

When ductile metals are subjected to large plastic strains, particularly at high strain rates ($\gtrsim 10^3\,\mathrm{s}^{-1}$), it is often found that the deformation pattern is not smooth and homogeneous, but shows marked localization of strain along narrow bands [1]. This phenomenon, called shear banding, has important implications since strain localization often acts as a prelude to material failure. This understandably has adverse repercussions for a material's ductility and integrity in deformation processing [2–4] and high-rate structural applications

Electronic supplementary material is available online at https://doi.org/10.6084/m9.figshare.c.5099326.

THE ROYAL SOCIETY
PUBLISHING

such as penetration and impact [5–7]. Clearly, a detailed understanding of shear band onset characteristics is of critical importance for both quantifying conditions required for banding and designing practical means to control it [6,8,9]. While most extensively studied in the context of polycrystalline metals, shear banding has been also widely observed in other material systems such as metallic glasses [10–13], polymers [14,15] and granular media [16,17].

The actual appearance of shear bands is dependent to some extent on the material itself, and comprehensive reviews of shear bands can be found in [1,18,19]. Nevertheless, recent *in situ* observations [20,21] suggest that the sequence of steps leading to a fully developed band with high strain localization in its vicinity can be demarcated into distinct stages of *nucleation* and *growth*, irrespective of the material system. During the nucleation stage, a strain inhomogeneity nucleates in an otherwise homogeneous strain field, followed by rapid propagation of its front to establish a thin and well-defined shear band interface across the whole specimen. The subsequent growth stage is characterized by accumulation of large plastic strains in the immediate vicinity of this interface, while regions away from the band essentially slide as rigid bodies. In this picture, the minimum shear stress required to nucleate a thin interface may be regarded as the nucleation stress, and stress that drives the localized flow development as the growth stress, of shear bands themselves [22].

The present article is concerned with understanding the nucleation properties of shear bands in ductile metals, with a specific focus on nucleation stresses. Although considerable progress has been made in modelling shear band nucleation and propagation aspects [23–26], direct experimental characterization of band nucleation has proved a difficult problem. This is primarily because high strain rate loading configurations (e.g. impact and explosive loading) typically used to study shear banding are not suited for the isolation of single bands. Furthermore, the small time scales (typically a few microseconds) involved in band nucleation pose additional experimental challenges. As a result, measurements of band nucleation properties (dynamics, stresses, etc.) in metals have been quite limited. It may be also noted that, even in metallic glasses where shear band nucleation stresses are often reported, stresses are not directly measured but usually extracted from nanoindentation tests [27–29].

In our prior work, we have devised a novel two-dimensional (2D) shear configuration wherein isolated shear bands can be formed and examined independently without interfering effects from other bands [20,22]. This has enabled *in situ* observations of single shear bands and elucidated several key features of shear banding such as band nucleation, propagation kinetics and kinematics of localized flow (boundary layer) evolution during the secondary growth stage [21].

In the present study, using this configuration, we probe nucleation properties of isolated shear bands in three different model, low melting point alloys. *In situ* high-speed imaging and force measurements are used to decouple shear band nucleation from the subsequent growth stage and thereby accurately determine equivalent stresses. The principal finding that emerges from our study is that the band nucleation stress τ_C is a material-dependent constant that is insensitive to external loading conditions and $\approx 0.05\mu_0$, with μ_0 being the shear modulus. A transition in the flow pattern from shear banding to homogeneous type at stress levels below τ_C is also unambiguously demonstrated using our *in situ* flow observations. Based on the results, phase diagrams demarcating shear banding and homogeneous flow modes are constructed.

The remainder of this article is organized as follows. The shear loading setup, imaging methods and material systems used in the study are described in §2. *In situ* observations of shear band dynamics and calculation of nucleation stresses are presented in §3. The transition between shear banding and homogeneous flow modes and phase diagrams showing where each of these regimes occur are also presented in that section. Implications of the findings and a microscopic interpretation of shear band nucleation as a mechanical instability involving sudden breakdown of dislocation barriers are discussed in §4. Concluding remarks are presented in §5.

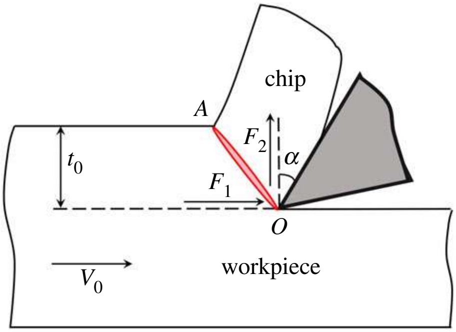

Figure 1. Schematic of 2D cutting configuration used to impose large strain shear deformation. The deformation zone (*OA*) where plastic shearing occurs, as the material is transformed into a chip, is highlighted in red. Two orthogonal force components, F_1 and F_2, acting on the tool are shown, along with the experimental parameters (α, V_0 and t_0). (Online version in colour.)

2. Experimental

The loading configuration used to study shear bands is a 2D (plane strain) cutting configuration, as shown in figure 1. In this configuration, material is subjected to nominal simple shear in a narrow deformation zone (red shaded area *OA*, figure 1) as a thin layer of material of predefined thickness t_0 is removed in the form of a chip by a sharp wedge-shaped tool. The tool inclination α (figure 1) controls the level of imposed shear strain (γ), while the strain rate ($\dot{\gamma}$) in the deformation zone is primarily determined by the deformation velocity V_0. For instance, shear strains in the range of 1–5 and strain rates from 10 to $10^5\,\mathrm{s}^{-1}$ can be conveniently accessed by controlling these parameters. More importantly, for the present purposes, this shear configuration allows the formation of isolated shear bands, i.e. one at a time and at an *a priori* known location (tool tip) [21,22]. This feature is central to the present study as it allows shear band nucleation to be directly examined *in situ*. Furthermore, a large number of shear bands (> 200) can be generated in a single experiment or 'cut', which offers additional benefits in regards to data repeatability verification and statistical analysis of band nucleation attributes such as stresses and propagation velocity. Some of these unique aspects of the cutting geometry in relation to shear bands appear to have been recognized more than 50 years ago by Recht [30]. Several recent studies [31–33] also suggest a renewed interest in utilizing cutting–deformation framework for studying large strain deformation phenomena, including shear banding, flow instabilities and ductile fracture. Similar 2D configurations have also proved invaluable for isolating frictional wave phenomena at soft adhesive interfaces [34].

The material systems studied are three low melting point (T_m) bismuth-based eutectic alloys (labelled Alloys 1–3) with melting points of 47°C, 70°C and 138°C, respectively. The nominal composition and thermophysical properties of these alloys are presented in table 1. The choice of these alloys was governed by the fact that they exhibit shear banding at strain rates multiple orders smaller than the typical rates ($> 10^3\,\mathrm{s}^{-1}$) at which banding occurs in engineering alloys such as Ti and steels [21]. This means that shear band dynamics can be studied *in situ* at high resolution, both spatially and temporally, which is highly difficult, if not impossible, to achieve in conventional high T_m materials. Furthermore, the deformation behaviour of these alloys under ambient temperature conditions is such that the flow stress is highly sensitive to the strain rate, with little dependence on strain; for example, see compression test data provided in figure S1 (electronic supplementary material). In all three alloys, the ambient temperature flow stress σ varies with effective strain rate ($\dot{\epsilon}$) roughly as: $\sigma \propto \dot{\epsilon}^m$, where m is in the range of 0.06–0.13 (depending on the alloy). It is important to note that this type of highly rate-dependent behaviour (with negligible strain hardening) is a common characteristic of metals deforming at very high strain rates, typically $> 10^3\,\mathrm{s}^{-1}$ [35]. Therefore, low T_m alloys are attractive model materials to

Table 1. Thermophysical properties of low melting point alloys at 23°C.

properties	Alloy 1	Alloy 2	Alloy 3
melting point (T_m)	47°C	70°C	138°C
composition (wt. %)	44.7Bi, 22.6Pb, 19.1In, 8.3Sn, 5.3Cd	50Bi, 26.7Pb, 13.3Sn, 10Cd	58Bi, 42Sn
density (ρ)	8.98×10^3 kg m^{-3}	9.26×10^3 kg m^{-3}	8.15×10^3 kg m^{-3}
thermal diffusivity (κ)	0.09×10^{-4} m^2 s^{-1}	0.14×10^{-4} m^2 s^{-1}	0.14×10^{-4} m^2 s^{-1}
specific heat (C)	180.6 W s kg^{-1} K^{-1}	165.7 W s kg^{-1} K^{-1}	167.7 W s kg^{-1} K^{-1}
thermal conductivity (k)	14.4 W m^{-1} K^{-1}	21.5 W m^{-1} K^{-1}	19.4 W m^{-1} K^{-1}
strain rate sensitivity (m)	0.12	0.13	0.06

experimentally ‘simulate’ the most essential features of high strain rate behaviour of metals (including shear banding) at low deformation speeds.

The materials were obtained from Belmont Metals Inc. (Brooklyn, NY) in the form of ingot and cast into the desired shape and size by preheating the metal to 200°C and pouring into a rectangular-shaped aluminium mould (∼ 75 mm × 25 mm × 2 mm). Wood’s metal (Alloy 2, $T_m = 70°$C) was chosen as the prototypical material in most of the experiments. The shearing experiments were carried out using a freshly ground high-speed steel tool (edge radius ∼ 5 µm) at different V_0 in the range of 0.005–10 mm s^{-1}. This corresponds to a strain rate variation over four orders of magnitude from ∼ 0.1 to 10^3 s^{-1}. t_0 was kept in the range of 150 to 500 µm and α between $-20°$ and $+40°$. The effects of ambient temperature were studied by performing experiments at different pre-heat/cool temperatures (T_0) from −20°C to 65°C. In these experiments, both the sample and tool-holder assembly were maintained at the desired temperature using dry ice or a heat gun.

In all the experiments, force components parallel and perpendicular to V_0 direction (figure 1) were measured using a piezoelectric force sensor (Kistler 9129AA) mounted directly under the tool. These measurements were used for stress calculations.

Direct time-resolved observations of the plastic flow were made using a high-speed CMOS camera (pco dimax HS4), synchronized with the force sensor. The plane strain condition at the specimen side surface being imaged was ensured by lightly constraining this side using a transparent sapphire plate and imaging through this plate [21]. The spatial resolution of our imaging was 0.98 µm (per pixel). Although the camera is capable of recording image sequences up to 50 000 frames per second, frame rates with a 100–200 µs interframe time (depending on V_0) were found to be adequate for capturing the shear band dynamics, given the low deformation speeds under which shear bands can be produced in low T_m alloys [21]. Quantitative full-field displacement data were obtained by analysing the high-speed image sequence using a correlation-based image processing method called particle image velocimetry (PIV) [36]. By using the PIV displacement data, the plastic flow field characteristics were analysed using streaklines, grid deformation, strain and strain rate maps. This imaging and image analysis also enabled us to establish direct correlations between the macroscopic force traces and shear band dynamics at the mesoscale. A detailed description of our experimental setup and full-field deformation analysis can be found in [21].

3. Results

In situ imaging, image analysis and force measurements have provided complete characterization of the shear band dynamics and enabled measurements of nucleation stresses across different strain rates and temperatures.

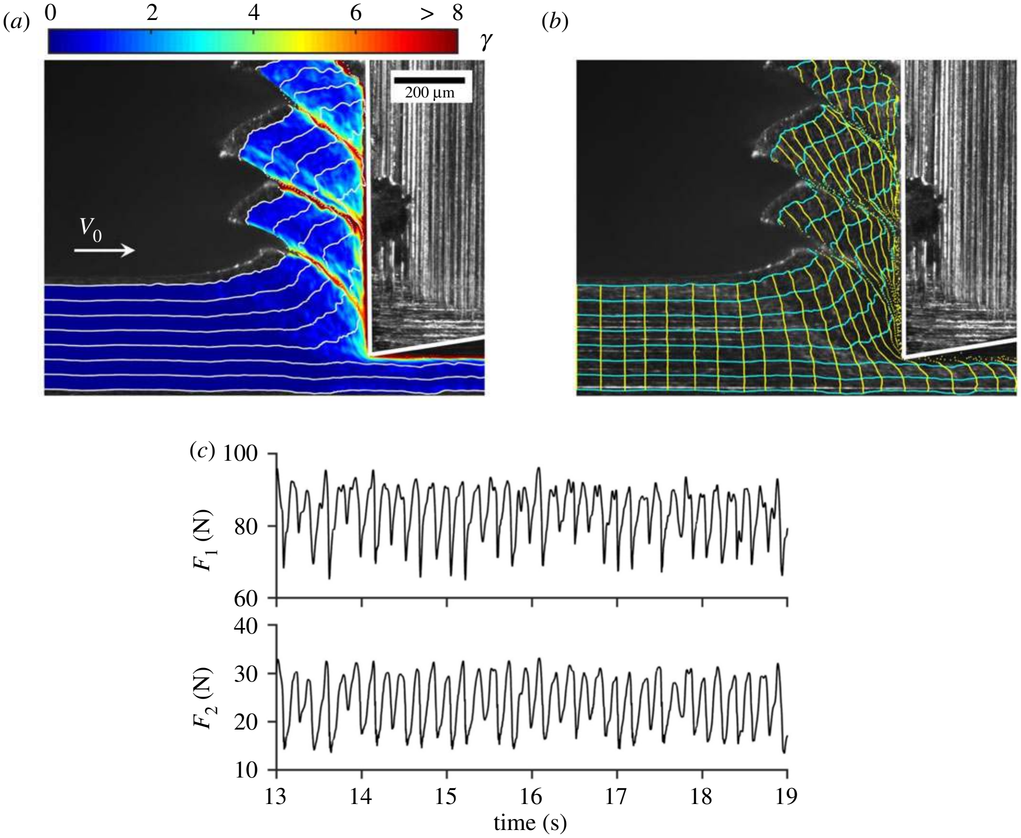

Figure 2. Shear banding characteristics at $V_0 = 1.5\,\mathrm{mm\,s^{-1}}$: (*a*) shear strain field and (*b*) artificial grid superimposed on the high-speed image showing a highly heterogeneous plastic flow characterized by high strain shear bands and surrounding low-strain regions. (*c*) The corresponding force versus time plot, where each oscillation in the force trace represents single shear band formation. (Online version in colour.)

(a) General attributes of shear banding

We begin with a synopsis of the primary experimental observations pertaining to shear band attributes and their dynamics. Figure 2 shows a snapshot of a typical experiment ($\alpha = 0°$, $t_0 = 250\,\mu\mathrm{m}$) where the flow is dominated by periodic shear banding. In this experiment, $V_0 = 1.5\,\mathrm{mm\,s^{-1}}$, which corresponds to a nominal strain rate of $\sim 50\,\mathrm{s^{-1}}$. Figure 2*a* shows the PIV-measured shear strain field and streaklines (white lines) superimposed on a high-speed image. The deformed material (chip) is clearly characterized by two distinct regions—thin bands of high strain separated by low-strain segments. The typical shear band strain is ~ 8, an order of magnitude higher than in the surrounding regions. The large strain localization within shear bands is shown in figure 2*b*, which shows an artificial deformed grid on top of the image. This was obtained by initially overlapping a square grid ($40\,\mu\mathrm{m} \times 40\,\mu\mathrm{m}$) on the undeformed workpiece and tracking/updating each point on the grid lines during the deformation process. The stark contrast in the extent of deformation between shear bands and surrounding regions is evident. While the band material is highly sheared, as can be judged based on relative positions of streaklines (cyan colour, figure 2*b*) on either side of the band, material segments in between the bands are only slightly distorted. It should be also noted that shear bands seen here are macroscopic, in the sense that they traverse across the entire specimen width (dimension normal to the viewing plane in figure 2) [21].

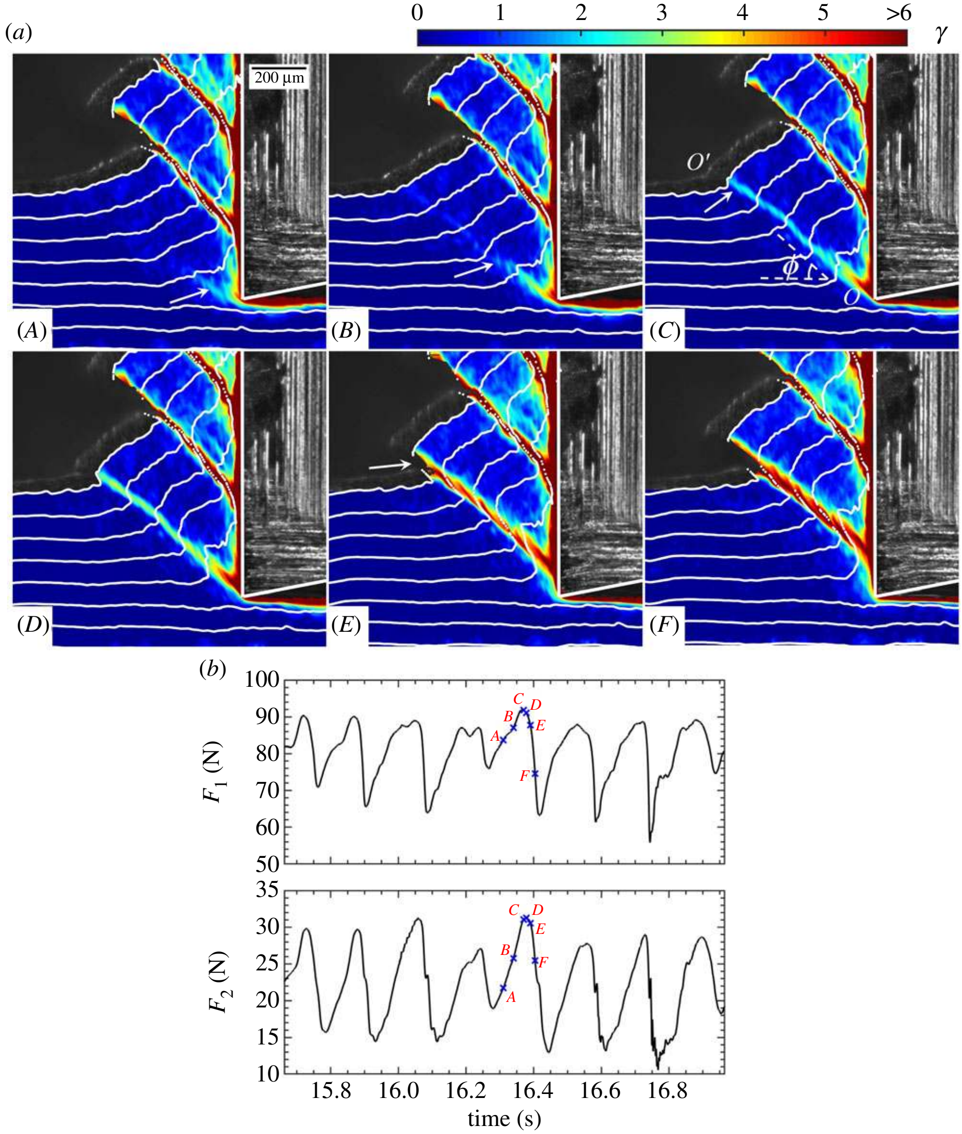

Figure 3. (*a*) High-speed image sequence showing formation of a single shear band at $V_0 = 1.5\,\mathrm{mm\,s^{-1}}$. Images show the shear strain field distribution along with streaklines. Frames *A*–*C* and *D*–*F* show the shear band initiation and sliding/growth phases, respectively. The time instances corresponding to individual frames are marked on the F_1 and F_2 force traces in (*b*). Arrow in frames *A*–*C* tracks the initiation of shear band, starting from its nucleation at tool tip (frame *A*) to propagation toward the material surface and formation of a thin interface OO' (see frame *C*). Formation of this interface OO' coincides with maximum in F_1. Large strain accumulation along the interface occurs during the second sliding phase (frames *D*–*F*) under a falling load. Except for a small crack near the free surface (see at arrow, frame *E*), material remains continuous along the shear band. (Online version in colour.)

The force versus time plot during shear banding is shown in figure 2*c*, with F_1 and F_2 being the horizontal and vertical forces, respectively. Synchronous high-amplitude oscillations are seen in both the directions, where each oscillation corresponds to the formation of a single band. That the oscillations (therefore, shear bands) are highly periodic and equally spaced in time suggests that banding is not a stochastic process. Importantly, the fact that shear bands form in a sequential manner, one at a time, affords opportunities for making time-resolved observations of single-band initiation and development.

Figure 3 shows six high-speed frames showing the evolution of a single shear band along with respective time instances on the force plot. Shear band evolves in two distinct stages of initiation and growth. Frames *A*–*C* show the first stage, involving nucleation of a localized strain inhomogeneity at the tool tip (frame *A*) and propagation of the band front towards the free surface (see arrow, frame *B*). By frame *C*, a very thin and well-defined band interface OO' traversing the entire specimen is established. At this stage, shear band strain is ~ 1 and band orientation is closely aligned with the maximum shear stress direction. For example, the band orientation ϕ with respect to V_0 is 34°, while the maximum shear direction calculated based on forces is 36°. It is also critical to note that the nucleation of band interface (frame *C*) coincides with the maximum in F_1 (see point *C* in figure 3*b*).

Frames *D*–*F* show the second growth stage of shear banding, characterized by accumulation of large strains in the immediate vicinity of band under a dropping load. As shown in figure 3, this strain accumulation along the shear band specifically occurs via relative 'sliding' of the material blocks on either side of the band plane OO' in equal and opposite directions. It is also important to note that, during this sliding process, the material remains continuous across the band despite large strains. It is only during the later stages of sliding that a crack forms at the free surface; for example, see arrow in frame *E*, where the broken streakline indicates material separation at this location. By frame *F*, it can be seen that large strain levels > 6 develop around the shear band, with the band also developing a characteristic thickness of $\sim 20\,\mu\text{m}$. The shear steps at the free surface are also developed during this sliding stage.

The sequence of steps leading to formation of a fully developed band is now clear. While the nucleation stage establishes band interface and orientation, the majority of the localized strains (80%) develop during the subsequent sliding/growth phase. Once the growth stage comes to a halt, marked by minimum in F_1, another band initiates in the neighbouring workpiece region, and the process is repeated.

We also note that the aforementioned two-stage mechanism of shear banding is not specific to the current model material systems, but has been observed also in other alloys including titanium, cold-worked brass and nickel-based superalloys [20]. In the present study, the two-stage mechanism was also confirmed under different conditions of V_0, α and t_0. *In situ* observations of banding at $\alpha = 20°$ can be found in figure S2 (electronic supplementary material), for comparison.

(b) Nucleation stresses

From the aforementioned *in situ* observations, it is clear that shear band nucleation, marking the onset of plastic instability, can be decoupled from the strain-intensive growth stage. Moreover, the fact that nucleation of a thin, well-defined band OO' (see frame *C*, figure 3) coincides with the peak in the primary force F_1 allows us to define and measure the characteristic nucleation stress (τ_C) required for its formation. τ_C calculation is illustrated using the force plot in figure 4, where force values at band initiation, $F_{1,C}$ and $F_{2,C}$, are marked using red circles and crosses, respectively. It may be noted here that while band initiation strictly coincides with the maximum in F_1, the peak in the tangential force F_2 occurs a little after band has initiated. Similar observations were made also in experiments at different α (see figure S2, electronic supplementary material). Based on $F_{1,C}$ and $F_{2,C}$, τ_C for each band can be thus obtained from the resultant shear force parallel to band and band area. The normal stress σ_C acting on the band during its initiation can be similarly derived from the resultant normal force. Mathematically

$$\left.\begin{aligned} \tau_C &= \frac{F_{\text{shear}}}{A_S} = \frac{(F_{1,C}\cos\phi - F_{2,C}\sin\phi)\sin\phi}{bt_0} \\ \text{and}\qquad \sigma_C &= \frac{F_{\text{norm}}}{A_S} = \frac{(F_{1,C}\cos\phi + F_{2,C}\sin\phi)\sin\phi}{bt_0}, \end{aligned}\right\} \tag{3.1}$$

where F_{shear} and F_{norm} are the resolved shear and normal forces, respectively, $A_S = bt_0/\sin\phi$ is the area of a freshly nucleated band, b is the thickness dimension of the sample and ϕ as before is band orientation with respect to V_0 (figure 3). Measurements over some 200+ bands produced under

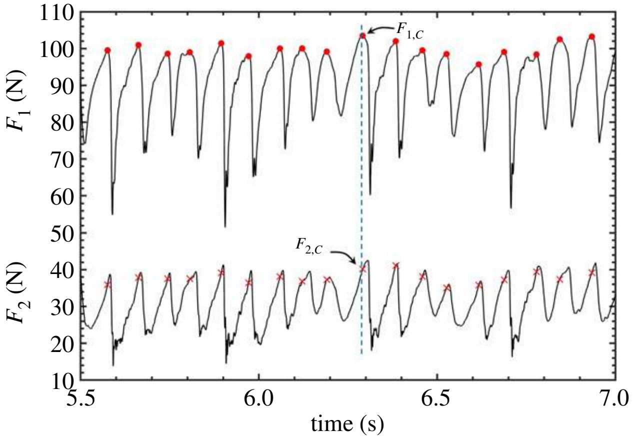

Figure 4. Typical force trace associated with shear banding ($V_0 = 4\,\text{mm s}^{-1}$, $\alpha = 0°$). Each oscillation in F_1 and F_2 represents single shear band cycle. $F_{1,C}$ and $F_{2,C}$ represent the forces at band nucleation and are marked using red circles and crosses, respectively. Average shear band nucleation stress (τ_C) in each experiment was determined from $F_{1,C}$ and $F_{2,C}$ values collected over multiple bands (see text for details). (Online version in colour.)

identical conditions as in figure 3 show that τ_C is 71 ± 2 MPa, while σ_C is 91 ± 3 MPa. Note that in equation (3.1), we do not consider the inertial force components that usually arise in cutting due to momentum changes across the deformation zone [37,38]. While this approximation is justified at relatively low speeds used in the present work (given that the inertial forces are about 8–10 orders of magnitude lower than the deformation forces F_1 and F_2), one should be careful to consider the inertial effects at high cutting speeds $\gtrsim 10\,\text{m s}^{-1}$ [39].

Additional experiments over a wide range of testing parameters show that τ_C is likely a material constant. This is demonstrated in figure 5, where the force data (F_{shear} and F_{norm}) for band nucleation are plotted as a function of shear band A_S, for nearly 60 different experimental combinations of V_0, α and t_0. Also, for each experimental condition, force and area values reported are the average of at least 200 bands. From the F_{shear} versus A_S plot (figure 5*a*), it is startling to observe that all the points from various experiments fall on a single master line (black dashed line), whose slope is given by $\tau_C = 70$ MPa. It is also seen that any deviation in the linearity from this line is of the same order of the scatter in the force/area data itself. These observations make it clear that τ_C is an intrinsic material characteristic.

The dependence of F_{norm} on A_S is shown in figure 5*b*. It is evident that no single line can be drawn through the data, although it appears that points align themselves along different families depending on α. In contrast to single τ_C, σ_C varies over a 50–125 MPa range. Therefore, it appears that τ_C also bears no relationship to the normal stress component acting on the band plane. This is clearly akin to the critical resolved shear stress concept used in crystal plasticity for describing the dislocation slip onset [40]. In fact, additional experiments in the temperature range of −30°C to 60°C showed that τ_C remains independent of the ambient temperature and is about 0.05–0.06 times the corresponding shear modulus (μ_0) value, except close to the melting point where τ_C/μ_0 ratio was found to be somewhat higher at 0.08.

It is important to note that the aforementioned observations pertaining to τ_C are no mere coincidence or peculiar to the idiosyncrasies of Wood's metal since shear banding in the other two alloys investigated in this study was also characterized by a unique τ_C. Stress data for Alloy 1 ($T_m = 47°\text{C}$) and Alloy 3 ($T_m = 138°\text{C}$) are presented in table 2 at three different α ($V_0 = 1\,\text{mm s}^{-1}$). It is again of interest to note that each material is characterized by a characteristic τ_C regardless of the normal stress. While the τ_C values themselves are different depending on the alloy (~ 55 MPa for Alloy 1 and 86 MPa for Alloy 3), τ_C/μ_0 ratio was again found to be ≈ 0.05 in both the alloys. Although empirical in nature and tested only over a rather limited range of temperatures, these

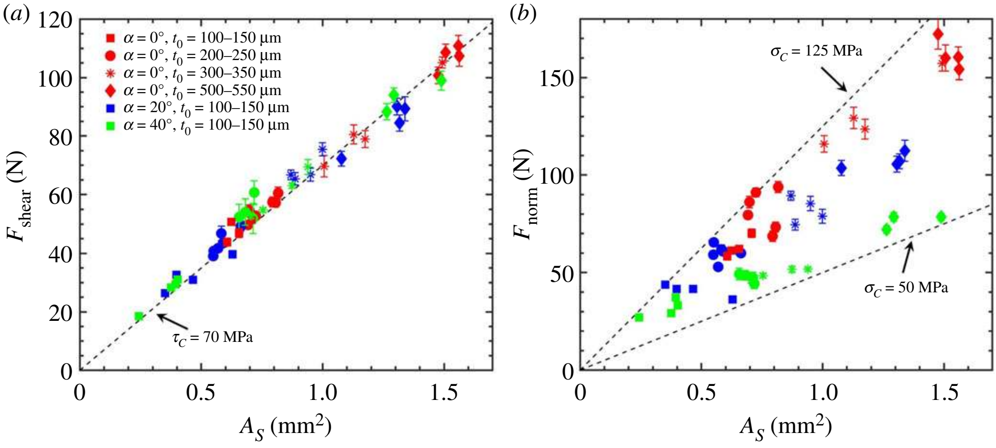

Figure 5. Shear band nucleation force data from over 60 different experiments, presented using (*a*) F_{shear} versus A_S and (*b*) F_{norm} versus A_S plots. Each point represents data obtained at a different combination of α, V_0 and t_0. Different colours: red, blue and green represent different α: 0°, 20° and 40°, respectively, while different symbols represent different t_0 ranges (see figure legend). In (*a*), all F_{shear} data fall on a single master line, regardless of the experimental parameters, indicating a constant shear stress at band nucleation. The best straight line fit, shown using the black dashed line, corresponds to $\tau_C = 70$ MPa. In contrast, F_{norm} data in (*b*) show a scattered distribution bounded between two straight lines corresponding to σ_C of 50 and 125 MPa. (Online version in colour.)

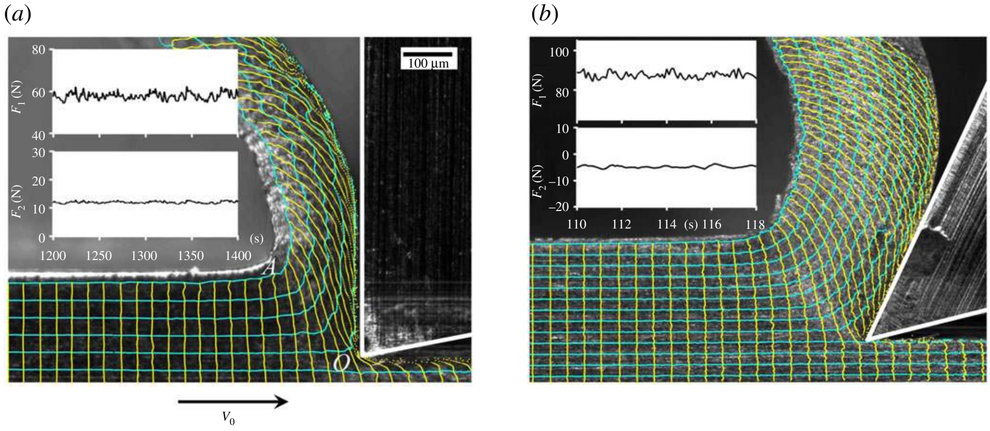

Figure 6. Homogeneous flow at lower strain rates of (*a*) 0.2 s^{-1} and (*b*) 1 s^{-1}. Homogeneous plastic flow devoid of localization is clearly evident in both the cases from the uniformly deformed grid pattern in the chip and steady-state force profiles (see insets). (Online version in colour.)

observations suggest a potential scaling relationship between τ_C and μ_0, similar to that between the theoretical strength and the modulus [41].

(c) Shear banding to homogeneous flow transition

The observation of constant τ_C over a range of conditions, coupled with the fact that the shear band plane coincides with the maximum shear direction, suggests a condition for banding onset based on maximum shear stress. This also suggests a transition in the flow mode to homogeneous type when the shearing stress τ is $< \tau_C$. This transition was explored in our experiments by

Table 2. Nucleation stress data for the three alloys at different α. Values reported in the table are the average and one standard deviation calculated from multiple shear bands. $V_0 = 1\,\text{mm s}^{-1}$.

	$\alpha = 0^\circ$	$\alpha = 20^\circ$	$\alpha = 40^\circ$
Alloy 1	$\sigma_C = 105 \pm 4$ MPa, $\tau_C = 52 \pm 3$ MPa	$\sigma_C = 79 \pm 2$ MPa, $\tau_C = 56 \pm 2$ MPa	$\sigma_C = 68 \pm 3$ MPa, $\tau_C = 57 \pm 2$ MPa
Alloy 2	$\sigma_C = 115 \pm 3$ MPa, $\tau_C = 72 \pm 2$ MPa	$\sigma_C = 103 \pm 4$ MPa, $\tau_C = 74 \pm 2$ MPa	$\sigma_C = 62 \pm 4$ MPa, $\tau_C = 73 \pm 7$ MPa
Alloy 3	$\sigma_C = 222 \pm 8$ MPa, $\tau_C = 92 \pm 4$ MPa	$\sigma_C = 136 \pm 6$ MPa, $\tau_C = 86 \pm 2$ MPa	$\sigma_C = 95 \pm 7$ MPa, $\tau_C = 86 \pm 4$ MPa

altering the material's shear flow stress using external strain rate and temperature as control parameters. As an example, figure 6 shows *in situ* observations of the plastic flow in Wood's metal, where the artificial grid (obtained using PIV flow analysis) is shown superimposed on the raw images. The loading condition in figure 6*a* is identical to that in figure 3, except that $V_0 = 0.01\,\text{mm s}^{-1}$ and the corresponding $\dot{\gamma} \sim 0.1\,\text{s}^{-1}$ are two orders lower. Figure 6*b* represents a similar example at $\alpha = 20^\circ$, where $\dot{\gamma}$ is $\sim 1\,\text{s}^{-1}$, about one order lower than in figure 3. A striking observation from these experiments is a different flow mode where the undeformed material transforms into a homogeneously deformed chip as the material passes through the plane *OA*. That the underlying flow is 'laminar' without localization can be seen from the smooth streaklines (horizontal cyan lines) and uniform deformation of the grid pattern over the entire chip sample. The PIV strain analysis also confirmed a uniform strain distribution in the chip, with the measured shear strains (γ) being close to 3.5 and 1.7, respectively, for figure 6*a*,*b*. Furthermore, this homogeneous flow mode is also accompanied by steady-state forces in both the orthogonal directions (F_1 and F_2). This is in stark contrast to the shear banding mode, where the force profiles are characterized by high-amplitude, periodic oscillations (figures 2 and 3).

It is important to note that the principal deformation process in figure 6 is also one of shear deformation confined along a thin zone/plane *OA*. This, for instance, can be clearly observed from the deformation of square grids into elongated rhomboid shapes as material exits the plane *OA* (figure 6). This in turn suggests that the material's shear flow stress τ along this plane can be estimated using measured forces. In fact, replacing $F_{1,C}$ and $F_{2,C}$ terms in equation (3.1) with steady-state forces F_1 and F_2, respectively, and ϕ with the shear plane orientation with respect to V_0, reduces τ_C calculation to τ for the steady-state homogeneous flow. This calculation shows that τ for the two cases shown in figure 6 are 52 MPa and 58 MPa, respectively, which are well below the critical τ_C required for band nucleation.

The transition between the two flow modes and corresponding stress attributes are further elaborated in figure 7 over a wider experimental dataset, where shear stresses are plotted as a function of V_0, for three different α values. An approximate boundary between shear banding and homogeneous flow modes is also marked in the figure using a vertical dashed line. In the case of homogeneous flow, stress plotted along the vertical axis represents τ under which material undergoes steady-state shearing, while for shear banding, it is the critical nucleation stress τ_C. It is shown in figure 7 that at small V_0, τ values are significantly lower than τ_C. For example, at $0.01\,\text{mm s}^{-1}$, $\tau \sim 40$ MPa, which is well below τ_C. As noted earlier, this is quite consistent with the occurrence of homogeneous flow at small V_0.

From figure 7, it can be seen that τ increases with V_0, and when $\tau \simeq \tau_C$ (horizontal dashed line) at V_0 of 0.3–1 mm s^{-1}, homogeneous flow gives way to shear banding. Within the shear banding domain, τ_C essentially remains constant slightly above 70 MPa irrespective of α or V_0, consistent with our earlier observations (figure 5). Together, these observations suggest a critical shear stress-based condition for the homogeneous flow to shear banding transition.

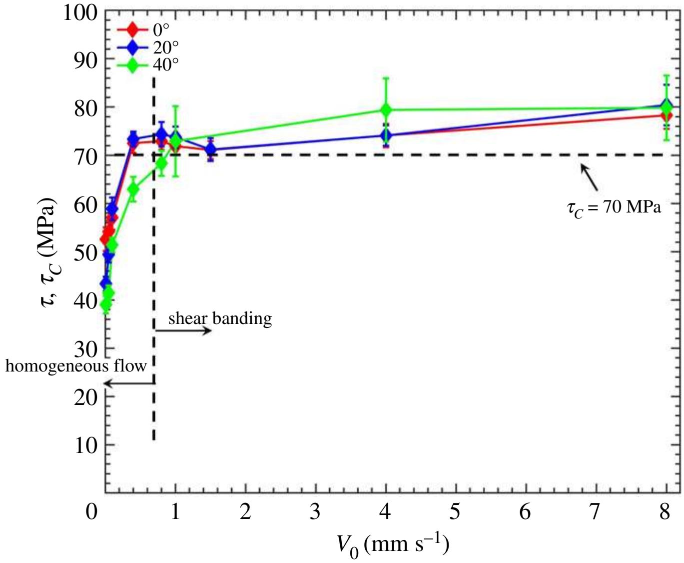

Figure 7. Shear stress data shown as a function of V_0 for different α (0°, 20° and 40°). Approximate boundary demarcating the homogeneous flow and shear banding modes is shown using a vertical black dashed line. Stress values correspond to shear flow stress (τ) for homogeneous flow and band nucleation stress (τ_C) in the case of shear banding. At low V_0 ($\lesssim 0.5$ mm s^{-1}), flow is homogeneous, with τ being highly sensitive to V_0. Transition to banding occurs when τ reaches a critical value of about 70 MPa, marked by a horizontal black dashed line. Inside the shear banding regime, τ_C remains independent of V_0 or α. (Online version in colour.)

Based on our experimental observations of the flow type, it is now possible to construct a phase diagram as shown in figure 8, where the occurrence of each flow mode can be delineated in terms of nominal strain (γ) and strain rate ($\dot{\gamma}$) conditions. The scattered points in the diagram are individual experimental runs performed at different combinations of α and V_0, corresponding to different combinations of γ and $\dot{\gamma}$. Homogeneous and shear banding modes are marked using blue circles and red squares, respectively, with corresponding τ or τ_C values (in MPa) given next to the symbols. As with the stresses, strain and strain rate data for homogeneous flow correspond to steady-state values, while for shear banding, they represent prelocalization values just before band nucleation. As shown in the phase diagram, the two flow modes can be clearly demarcated using a vertical dashed line, corresponding to a critical $\dot{\gamma}_C \sim 10\,\mathrm{s}^{-1}$. In our experiments, simultaneous homogeneous flow and shear band events are sometimes observed close to the cut-off $\dot{\gamma}_C$, but the region $\dot{\gamma} < \dot{\gamma}_C$ shows no shear banding at all, while $\dot{\gamma} > \dot{\gamma}_C$ invariably shows shear banding.

It is also of interest to note that in the region $\dot{\gamma} \simeq \dot{\gamma}_C$, $\tau \simeq \tau_C$, irrespective of the strain (figure 8). This is not surprising given the weak strain dependence noted for the present alloy (see figure S1, electronic supplementary material). Therefore, the critical stress condition for flow transition in the present case reduces to a critical rate condition (in the absence of temperature effects).

(d) Temperature effects

The ambient temperature effects on the flow transition and band nucleation characteristics were explored by performing experiments at different temperatures (T_0) between −20°C and 65°C. For Wood's metal, this temperature range corresponds to homologous temperatures (T_0/T_m) between 0.74 and 0.98. In these experiments, α was kept constant at 0°, while V_0 was varied between 0.005 and 3 mm s^{-1}. Corresponding strain rates are in the 0.1–100 s^{-1} range. Results from *in situ* observations of the flow are plotted using T_0 versus $\dot{\gamma}$ phase diagram, as shown in figure 9. As mentioned earlier, the blue circles and red squares represent the homogeneous flow

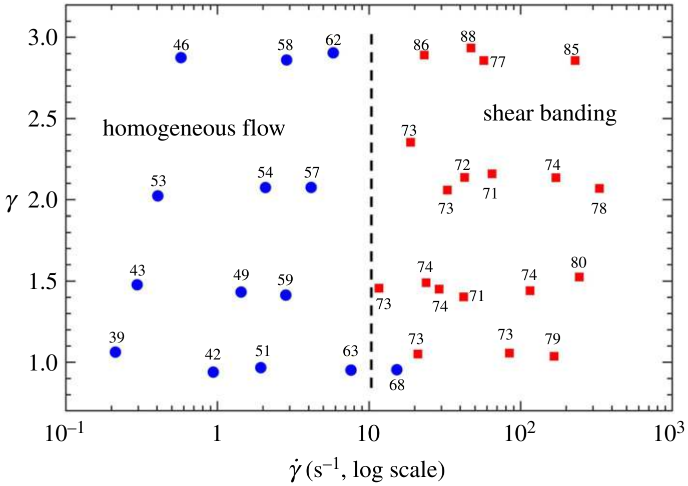

Figure 8. γ versus $\dot{\gamma}$ phase diagram showing the domains of homogeneous flow (blue circles) and shear banding (red squares) at ambient temperature ($T_0 = 298$ K). Individual points shown correspond to experiments performed at different combinations of α and V_0 (correspondingly, γ and $\dot{\gamma}$), while numerical values marked next to points are the corresponding τ or τ_C values in MPa. The approximate cut-off $\dot{\gamma}_C \simeq 10\,\text{s}^{-1}$ below which shear bands do not form is shown by the vertical dashed line. Stress values in the vicinity of this transition are seen to be close to 70 MPa. (Online version in colour.)

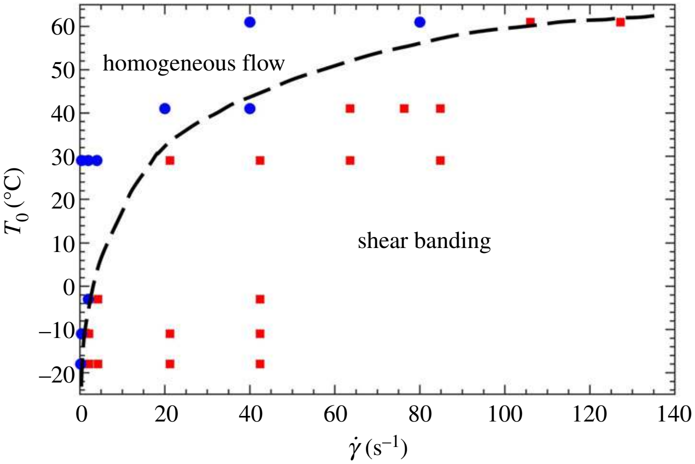

Figure 9. T_0 versus $\dot{\gamma}$ phase diagram showing the occurrence of homogeneous (blue circles) and shear banding (red squares) flow modes. The critical $\dot{\gamma}_C$ for flow transition is highly sensitive to temperature. This temperature dependence and an approximate boundary separating the flow modes are depicted using the curved black dashed line. (Online version in colour.)

and shear banding modes, respectively. It is clear from the phase diagram that temperature has a remarkable effect on the critical rate $\dot{\gamma}_C$ at which transition occurs. For example, decreasing the temperature to -3°C reduces $\dot{\gamma}_C$ to $1\,\text{s}^{-1}$, insomuch by an order of magnitude compared to the room temperature value. In fact, it was found that the critical rate at which flow transition occurs can be approximately described as $\dot{\gamma}_C \propto \exp(-1/T_0)$; see black dashed line in figure 9. We will discuss the origin of this exponential scaling in §4. However, for present purposes, it is sufficient to note that the measured τ values in the vicinity of this boundary were all found to be close to τ_C. This suggests that τ_C is also insensitive to T_0 at least in the investigated temperature range.

Note that in our study, deformation-induced plastic heating and associated temperature rise effects are minimized due to the low cutting speeds (with characteristic Péclet numbers $\ll 1$). That the temperature rise during cutting is small and no greater than 4–5°C even at the highest $V_0 = 10\,\mathrm{mm\,s^{-1}}$ has been established in our earlier study using thermocouple measurements [21]. Given that the maximum change in the flow stress due to this temperature rise, $\sim 2\,\mathrm{MPa}$, is sufficiently small, the plastic heating effects can be ignored in the present study.

Taken together with the observations shown in figures 7 and 8, this reaffirms that the exact strain, strain rate and temperature conditions that mark the flow transition are all governed by a common $\tau \simeq \tau_C$ condition.

4. Discussion

It is well established that the condition for intense strain localization along a shear band is that, following the initiation of a thin band plane somewhere in the material, the next increment of strain hardening is cancelled out by the accompanying material softening, mediated by either deformation-induced temperature rise [30,35] or other microstructural mechanisms [7,18]. The present study has focused on how such a thin plane is initiated in the first place.

Using *in situ* imaging of isolated shear bands, it is shown that shear band initiation occurs by nucleation of strain inhomogeneity at a stress concentration (tool tip in the present case, figure 3) followed by propagation of its front along the maximum shear direction. The end result is the formation of a thin, well-defined plane with a characteristic strain of ~ 1 and traversing the whole specimen; see figure 3. Our force measurements have further shown that there exists a minimum shear stress τ_C required for nucleating a band, with this stress being a physical characteristic of the material and proportional to the shear modulus. This is clearly brought out in our τ_C measurements over a wide range of experimental conditions (figure 5) and also demonstrated across three alloys with different melting points (table 2). At stress levels $< \tau_C$, a different flow mode—homogeneous flow—without shear bands occurs, which is also unambiguously established using our *in situ* experiments (figure 6). The domains where homogeneous and shear banding flow modes operate are illustrated using phase diagrams (figures 8 and 9).

The critical stress condition for the flow transition was demonstrated in figures 7 and 8 using direct stress measurements. Additional support for this condition from a physical standpoint is presented in figure 10, where the critical rate–temperature combinations marking the flow transition are plotted as $\log(\dot{\gamma})$ versus $1/T_0$. It is seen that all the data fall on a straight line, with the deviations being within experimental uncertainty. In fact, it turns out that a generalized thermoviscoplastic material with a flow stress dependence of the form $\tau \propto \{\dot{\gamma}\exp(Q/RT)\}^m$ [35] exhibits exactly this type of linear scaling between rate and temperature at a constant τ. In this picture, Q is the activation energy for plastic flow, R is the universal gas constant, and m as mentioned earlier is the rate sensitivity. For the data plotted in figure 10, the best straight line fit (black dashed line) is obtained at $\tau = 73\,\mathrm{MPa}$ and $Q = 42\,\mathrm{kJ\,mol^{-1}}$. Clearly, this τ is close to the τ_C measured independently in our other experiments (figure 5). Equally importantly, Q is close to the activation energy for self-diffusion for all the constitutive elements [42]. This is suggestive of an underlying plastic flow mechanism where the rate-controlling step is vacancy diffusion to or from the climbing dislocations held up at discrete obstacles [43].

Based on foregoing observations and analysis, a plausible microscopic mechanism by which a thin shear band plane nucleates can be now discussed. Consider, for instance, dislocation-mediated plastic flow connected with dislocation jumps across potential obstacles (e.g. precipitates, second-phase particles, forest dislocations), and let τ_C be the shear stress required to set the dislocation in motion around the obstacles in the absence of any thermal contribution. At temperatures above absolute zero, even if the applied stress is less than τ_C, dislocation can overcome the obstacle with the help of thermal fluctuations, provided sufficient time is made available for it to make the jump. However, at high strain rates, the specimen's internal plastic rate can lag the external displacement rate, and when stress reaches a critical value, one can envision breakdown of piled-up dislocations along a plane as a sudden 'burst'. In this

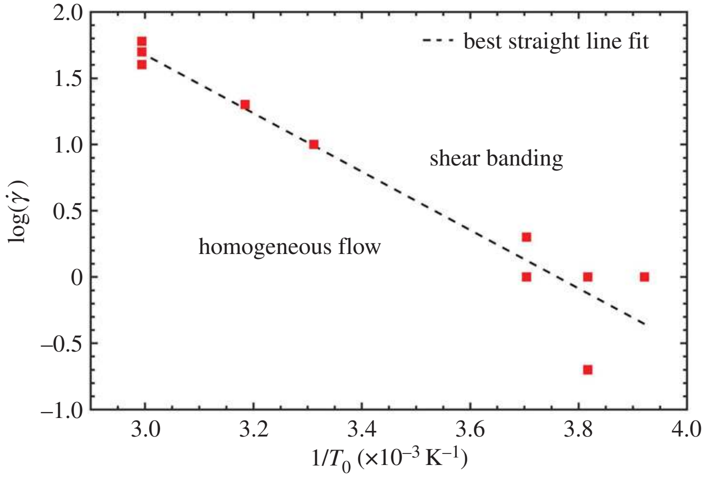

Figure 10. Log($\dot{\gamma}$) versus $1/T_0$ plot of the points close to the transition boundary in figure 9. The points are seen to closely fall on a single straight line, indicating that the critical $\dot{\gamma}_C$ for flow transition scales as $\exp(-1/T_0)$. The best straight line fit to the data is shown as a black dashed line. (Online version in colour.)

picture, such a breakdown corresponds to shear band nucleation at a critical τ_C. If the temperature rise or structural changes accompanying the pile-up breakthrough are such that they overcome the strain/strain rate hardening effect, strain localization results along a freshly nucleated band. While shear band initiation based on this type of dislocation pileup 'avalanche' mechanism has been postulated before by several authors [44–47] based on theoretical considerations, we believe our study provides the first quantitative experimental support in terms of activation energy and nucleation stress. It is of interest to note that the formation of microscopic slip bands is also known to be mediated by similar dislocation pile-up breakdown mechanisms [48].

It is noteworthy that the aforementioned microscopic description of shear band nucleation is consistent with our earlier observations that normal stresses play a little role in band nucleation, as expected for any dislocation-mediated process. Furthermore, the fact that τ_C scales with μ_0 is in line with the classical rate-dependent plasticity theory where the athermal stress component is often taken to be proportional to the shear modulus [43,49]. Importantly, this description also provides a unified explanation for several important observations related to shear banding in metals. For example, factors that promote shear banding such as multiphase or precipitation-hardened microstructures (as opposed to single phase) [50], very low temperatures [51], high deformation rates and high levels of cold-work [2]—all of which restrict dislocation motion—can be understood from the aforementioned dislocation basis. However, the precise mechanism of how dislocation slip that is confined to specific crystallographic planes can result in sample-scale bands that cut across several grains remains an open problem [52].

It is pertinent to also briefly discuss possible generalization of our results to other metals, beyond the model alloys investigated in this study. In this context, we compare our results with prior, albeit limited, data on band nucleation stresses. Using dynamic torsional experiments, Duffy's group reported τ_C values for steels in the range of 350–1100 MPa, depending on the material's microstructure, composition and prior heat treatment [50]. The corresponding τ_C/μ_0 ratios are between 0.01 and 0.02, substantially lower than that observed in the present study. It appears therefore that, as with regular dislocation nucleation [53], the activation energy, and therefore, characteristic stresses required for band nucleation depend considerably on the type and nature of the obstacles/barriers themselves. This hypothesis clearly requires additional study. However, our current work has established the correlation between band dynamics and the corresponding force trace (figure 3), so that τ_C measurements can be made across different material systems by merely observing the force traces, without need for detailed *in situ* imaging. Such measurements would be of practical value as they can be used in conjunction with the activation energies to predict the critical strain, strain rate and temperature conditions for the localized flow onset.

Finally, the dislocation Burgers vector and the fact that dislocations do not 'run away' after breaking through the obstacles but are characterized by a finite (stress-dependent) velocity [44] introduce intrinsic length and time scales into the band nucleation problem. In this regard, detailed examination of shear displacement profiles and band propagation velocities during shear band nucleation, and their possible connection with dislocation dynamics at the microscale, will be likely valuable for placing shear banding within a wider dislocation physics framework.

5. Conclusions

The nucleation of isolated shear bands in metals has been studied using a special shear loading configuration and *in situ* imaging using high-speed photography. This enabled band nucleation to be decoupled from the subsequent strain-intensive growth phase. Based on synchronous imaging and force measurements, the existence of a critical shear stress (τ_C) required for band nucleation was established across three different alloy systems. The independence of τ_C with regards to normal stresses, its constancy over a wide range of testing conditions and scaling with respect to the shear modulus (μ_0: $\tau_C \approx 0.05\mu_0$) were demonstrated. It is shown that these results can be rationalized from the viewpoint that shear band nucleation is a mechanical instability of the crystal lattice arising due to the sudden breakdown of dislocation barriers. A smooth, homogeneous flow mode without shear bands was reproduced at stress levels $< \tau_C$. Based on these observations, phase diagrams that delineate the strain rate, strain and temperature domains under which each of the flow modes (homogeneous versus shear banding) occur were developed. It is shown that the observed boundaries demarcating the two flow modes are consistent with $\tau \simeq \tau_C$ condition.

Data accessibility. Additional supporting data are available as electronic supplementary material.

Authors' contributions. S.Y. performed experiments and data analysis. Both the authors contributed to design of the study, interpretation of results, formulation of conclusions, writing and critical revisions of the manuscript. D.S. supervised the study. Both the authors approved the final version and agree to be accountable for all aspects of the work.

Competing interests. We declare we have no competing interest.

Funding. We acknowledge support from US DOE award DE-NA0003525 (via Sandia National Laboratories sub-award 2016312).

Acknowledgements. We would like to thank Harshit Chawla of Texas A&M University for his assistance with image processing and PIV analysis.

References

1. Dodd B, Bai Y. 2012 *Adiabatic shear localization: frontiers and advances*, 2nd edn. London, UK: Elsevier.
2. Hatherly M, Malin AS. 1984 Shear bands in deformed metals. *Scr. Metall.* **18**, 449–454. (doi:10.1016/0036-9748(84)90419-8)
3. Lapovok R, Tóth LS, Molinari A, Estrin Y. 2009 Strain localisation patterns under equal-channel angular pressing. *J. Mech. Phys. Solids* **57**, 122–136. (doi:10.1016/j.jmps.2008.09.012)
4. Azizi H, Zurob HS, Embury D, Wang X, Wang K, Bose B. 2018 Using architectured materials to control localized shear fracture. *Acta Mater.* **143**, 298–305. (doi:10.1016/j.actamat.2017.10.027)
5. Timothy SP, Hutchings IM. 1985 The structure of adiabatic shear bands in a titanium alloy. *Acta Metall.* **33**, 667–676. (doi:10.1016/0001-6160(85)90030-6)
6. Wright TW. 2002 *The physics and mathematics of adiabatic shear bands* (Cambridge Monographs on Mechanics). Cambridge, UK: Cambridge University Press.
7. Rittel D, Landau P, Venkert A. 2008 Dynamic recrystallization as a potential cause for adiabatic shear failure. *Phys. Rev. Lett.* **101**, 165501. (doi:10.1103/PhysRevLett.101.165501)

8. Rice JR. 1976 The localization of plastic deformation. In *Proc. 14th Int. Congress on Theoretical and Applied Mechanics* (ed. WT Koiter), pp. 207–220. Amsterdam, The Netherlands: North-Holland.
9. Burns T, Davies MA. 1997 Nonlinear dynamics model for chip segmentation in machining. *Phys. Rev. Lett.* **79**, 447–450. (doi:10.1103/PhysRevLett.79.447)
10. Donovan PE, Stobbs WM. 1981 The structure of shear bands in metallic glasses. *Acta Metall.* **29**, 1419–1436. (doi:10.1016/0001-6160(81)90177-2)
11. Lewandowski JJ, Greer AL. 2006 Temperature rise at shear bands in metallic glasses. *Nat. Mater.* **5**, 15–18. (doi:10.1038/nmat1536)
12. Jiang MQ, Dai LH. 2009 On the origin of shear banding instability in metallic glasses. *J. Mech. Phys. Solids* **57**, 1267–1292. (doi:10.1016/j.jmps.2009.04.008)
13. Jiang MQ, Dai LH. 2011 Shear-band toughness of bulk metallic glasses. *Acta Mater.* **59**, 4525–4537. (doi:10.1016/j.actamat.2011.03.075)
14. Bowden PB, Raha S. 1970 The formation of micro shear bands in polystyrene and polymethylmethacrylate. *Philos. Mag.* **22**, 463–482. (doi:10.1080/14786437008225837)
15. Fleck NA, Stronge WJ, Liu JH. 1990 High strain-rate shear response of polycarbonate and polymethyl methacrylate. *Proc. R. Soc. Lond. A* **429**, 459–479. (doi:10.1098/rspa.1990.0069)
16. Palmer AC, Rice JR. 1973 The growth of slip surfaces in the progressive failure of over-consolidated clay. *Proc. R. Soc. Lond. A* **332**, 527–548. (doi:10.1098/rspa.1973.0040)
17. Walley SM. 2012 Strain localization in energetic and inert granular materials. In *Adiabatic shear localization: frontiers and advances* (eds. B Dodd, Y Bai), pp. 267–310. London, UK: Elsevier.
18. Antolovich SD, Armstrong RW. 2014 Plastic strain localization in metals: origins and consequences. *Prog. Mater. Sci.* **59**, 1–160. (doi:10.1016/j.pmatsci.2013.06.001)
19. Walley SM. 2007 Shear localization: a historical overview. *Metall. Mater. Trans. A* **38**, 2629–2654. (doi:10.1007/s11661-007-9271-x)
20. Sagapuram D, Viswanathan K, Mahato A, Sundaram NK, M'Saoubi R, Trumble KP, Chandrasekar S. 2016 Geometric flow control of shear bands by suppression of viscous sliding. *Proc. R. Soc. A* **472**, 20160167. (doi:10.1098/rspa.2016.0167)
21. Yadav S, Sagapuram D. 2020 *In situ* analysis of shear bands and boundary layer formation in metals. *Proc. R. Soc. A* **476**, 20190519. (doi:10.1098/rspa.2019.0519)
22. Sagapuram D, Viswanathan K. 2018 Evidence for Bingham plastic boundary layers in shear banding of metals. *Extrem. Mech. Lett.* **25**, 27–36. (doi:10.1016/j.eml.2018.10.002)
23. Cherukuri HP, Shawki TG. 1997 On shear band nucleation and the finite propagation speed of thermal disturbances. *Int. J. Solids Struct.* **34**, 435–450. (doi:10.1016/S0020-7683(96)00019-4)
24. Grady DE. 1992 Properties of an adiabatic shear-band process zone. *J. Mech. Phys. Solids* **40**, 1197–1215. (doi:10.1016/0022-5096(92)90012-Q)
25. Bigoni D, Dal Corso F. 2008 The unrestrainable growth of a shear band in a prestressed material. *Proc. R. Soc. A* **464**, 2365–2390. (doi:10.1098/rspa.2008.0029)
26. Bordignon N, Piccolroaz A, Dal Corso F, Bigoni D. 2015 Strain localization and shear band propagation in ductile materials. *Front. Mater.* **2**, 22. (doi:10.3389/fmats.2015.00022)
27. Packard CE, Schuh CA. 2007 Initiation of shear bands near a stress concentration in metallic glass. *Acta Mater.* **55**, 5348–5358. (doi:10.1016/j.actamat.2007.05.054)
28. Perepezko JH, Imhoff SD, Chen MW, Wang JQ, Gonzalez S. 2014 Nucleation of shear bands in amorphous alloys. *Proc. Natl Acad. Sci. USA* **111**, 3938–3942. (doi:10.1073/pnas.1321518111)
29. Wang L, Lu ZP, Nieh TG. 2011 Onset of yielding and shear band nucleation in an Au-based bulk metallic glass. *Scr. Mater.* **65**, 759–762. (doi:10.1016/j.scriptamat.2011.07.022)
30. Recht RF. 1964 Catastrophic thermoplastic shear. *J. Appl. Mech.* **31**, 186–193. (doi:10.1115/1.3629585)
31. Yeung H, Viswanathan K, Compton WD, Chandrasekar S. 2015 Sinuous flow in metals. *Proc. Natl Acad. Sci. USA* **112**, 9828–9832. (doi:10.1073/pnas.1509165112)
32. Guo Y, Compton WD, Chandrasekar S. 2015 *In situ* analysis of flow dynamics and deformation fields in cutting and sliding of metals. *Proc. R. Soc. A* **471**, 20150194. (doi:10.1098/rspa.2015.0194)
33. Zeng F, Jiang MQ, Dai LH. 2018 Dilatancy induced ductile–brittle transition of shear band in metallic glasses. *Proc. R. Soc. A* **474**, 20170836. (doi:10.1098/rspa.2017.0836)
34. Viswanathan K, Sundaram NK, Chandrasekar S. 2016 Stick-slip at soft adhesive interfaces mediated by slow frictional waves. *Soft Matter* **12**, 5265–5275. (doi:10.1039/C6SM00244G)
35. Zener C, Hollomon JH. 1944 Effect of strain rate upon plastic flow of steel. *J. Appl. Phys.* **15**, 22–32. (doi:10.1063/1.1707363)

36. Adrian RJ, Westerweel J. 2010 *Particle image velocimetry*. Cambridge, MA: Cambridge University Press.
37. Shaw MC. 1989 *Metal cutting principles*. Oxford, UK: Oxford University Press.
38. Albrecht P. 1965 Dynamics of the metal-cutting process. *J. Eng. Industry* **87**, 429–441. (doi:10.1115/1.3670857)
39. Recht RF. 1985 A dynamic analysis of high-speed machining. *J. Eng. Industry* **107**, 309–315. (doi:10.1115/1.3186003)
40. Cottrell AH. 1953 *Dislocations and plastic flow in crystals*. New York, NY: Oxford University Press.
41. Kelly A. 1966 *Strong solids*. Oxford, UK: Oxford University Press.
42. Belchuk M, Watt D, Dryden J. 1990 Determining a constitutive equation for creep of a Wood's metal model material. In *Constitutive laws of plastic deformation and fracture* (eds AS Krausz, JI Dickson, J-PA Immarigeon, W Wallace), pp. 189–195. Dordrecht, The Netherlands: Springer. (doi:10.1007/978-94-009-1968-6_21)
43. Kocks UF, Argon AS, Ashby MF. 1975 *Thermodynamics and kinetics of slip*. Progress in Materials Science, vol. 19. Oxford, UK: Pergamon Press.
44. Gilman JJ. 1994 Micromechanics of shear banding. *Mech. Mater.* **17**, 83–96. (doi:10.1016/0167-6636(94)90051-5)
45. Armstrong RW, Elban WL. 1989 Temperature rise at a dislocation pile-up breakthrough. *Mater. Sci. Eng. A* **122**, L1–L3. (doi:10.1016/0921-5093(89)90642-4)
46. Hirth JP. 1992 A model for a propagating shear band on the basis of a tilt wall dislocation array. *Appl. Mech. Rev.* **45**, 71–74. (doi:10.1115/1.3121393)
47. Coffey CS. 1989 A prototypical model of a dislocation source capable of generating shear band structures in crystalline solids during shock or impact. *J. Appl. Phys.* **66**, 1654–1657. (doi:10.1063/1.344380)
48. Nabarro FRN. 1967 *Theory of crystal dislocations*. Mineola, NY: Dover Publications Inc.
49. Campbell JD, Ferguson WG. 1970 The temperature and strain-rate dependence of the shear strength of mild steel. *Philos. Mag.* **21**, 63–82. (doi:10.1080/14786437008238397)
50. Duffy J, Chi YC. 1992 On the measurement of local strain and temperature during the formation of adiabatic shear bands. *Mater. Sci. Eng. A* **157**, 195–210. (doi:10.1016/0921-5093(92)90026-W)
51. Basinski ZS. 1957 The instability of plastic flow of metals at very low temperatures. *Proc. R. Soc. A* **240**, 229–242. (doi:10.1098/rspa.1957.0079)
52. Brown LM. 2005 Dislocation pile-ups, slip-bands, ellipsoids, and cracks. *Mater. Sci. Eng. A* **400**, 2–6. (doi:10.1016/j.msea.2005.03.043)
53. Borovikov V, Mendelev MI, King AH. 2017 Effects of solutes on dislocation nucleation from grain boundaries. *Int. J. Plast.* **90**, 146–155. (doi:10.1016/j.ijplas.2016.12.009)